Low Temperature Physics/Fizika Nizkikh Temperatur, 2012, v. 38, No. 5, pp. 531–537

Evidence for Griffiths phase in multiferroic $BiMnO_3$ and $BiFe_{0.5}Mn_{0.5}O_3$ films

V.G. Prokhorov and G.G. Kaminsky

Institute of Metal Physics, NASU, Kiev 03142, Ukraine
E-mail: pvg@imp.kiev.ua

J.M. Kim, Y.J. Yoo, and Y.P. Lee

q-Psi and Department of Physics, Hanyang University, Seoul 133-791, Korea

V.L. Svetchnikov

National Center for HREM, TU Delft 2628AL, The Netherlands

G.G. Levchenko, Yu.M. Nikolaenko, and V.A. Khokhlov

Donetsk Institute for Physics and Technology, NASU, Donetsk 83114, Ukraine

Received December 15, 2011

Microstructure and magnetic properties of the $BiMnO_3$ and $BiFe_{0.5}Mn_{0.5}O_3$ films, prepared by the rf magnetron sputtering on $LaAlO_3$ (001) single-crystalline substrate, have been investigated. The selected-area electron diffraction analysis allows us to indentify the crystal structure of the $BiMnO_3$ film as an orthorhombic one while the $BiFe_{0.5}Mn_{0.5}O_3$ film has a hexagonal lattice symmetry. The high-resolution electron microscopy study reveals the presence of strip-domain phase with a periodic spacing of about 3*c* in both films. The magnetic measurements show that in addition to the basic paramagnetic phase, the films manifest the Griffiths phase behavior in a wide temperature range. We argue that the observed weak ferromagnetism is provided by an appearance of the strip-domain layered inclusions rather than the intrinsic physical origin of the films.

PACS: *68.05.cf* Liquid–liquid interface structure: measurements and simulations;
75.50.Bb Fe and its alloys;
75.50.Dd Nonmetallic ferromagnetic materials;
75.60.Ej Magnetization curves, hysteresis, Barkhausen and related effects.

Keywords: multiferroics, thin films, crystal structure, Griffiths phase.

1. Introduction

Multiferroics have attracted considerable attention due to their interesting fundamental science, connected with simultaneous effects of ferroelectric and magnetic order, and potential for applications in information storage, such as spintronic devices and sensors. Among the most studied single-component multiferroic compounds are the bismuth ferrite and the bismuth manganite, $BiFeO_3$ and $BiMnO_3$. The first of them is a canted *G*-type antiferromagnet (AFM) with the Néel point $T_N \simeq 643$ K, the ferroelectric transition temperature $T_C \simeq 1103$ K [1–4], and the weak ferromagnetic (FM) moment ($\simeq 0.02\ \mu_B$ / Fe) [5], which is arisen from the antisymmetric Dzyaloshinskii–Moriya (DM) exchange [6,7]. At the same time, the enhancement in FM response assumes importance because such improvement can help in utilizing of this compound for practical applications. From this standpoint $BiMnO_3$ is a more suitable compound due to an appearance of the FM order at $T_C \simeq 105$ K [8] and the ferroelectric polarization at $T_C \simeq 450$ K [9–11]. However, the measured ferroelectric effect for this compound is much smaller than the result calculated from first principle [12], making it difficult to associate the measured hysteresis loops to bulk ferroelectricity. Recent efforts to improve the ferroelectric and ferromagnetic properties of the considered multiferroics are

focused on the preparation of the $BiFeO_3$–$BiMnO_3$ alloy systems [13–18], which are very promising for a practical implementation. On the other hand, an influence of the crystal-lattice symmetry, the microstructure topology and the accumulated lattice strain, provided by an epitaxial growth of the films, on magnetic and ferroelectric properties of this multiferroic system has not been adequately studied.

In this paper we report the experimental results for $BiMnO_3$ (BMO) and $BiFe_{0.5}Mn_{0.5}O_3$ (BFMO) films deposited on $LaAlO_3$ (LAO) (001) single-crystalline substrate. The peculiarities of crystal structure and magnetic behavior are discussed in detail.

2. Experimental techniques

The films were prepared by rf magnetron sputtering at a substrate temperature of 650 °C [19]. To avoid the influence of lattice strain, accumulated during deposition, the all films were annealed at 900 °C for 2 h in air. The thickness of the films was $d \simeq 160$ nm. The high-resolution electron-microscopy (HREM) and the electron-diffraction (ED) studies were carried out using a Philips CM300UT-FEG microscope with a field emission gun operated at 300 kV. The point resolution of the microscope was in the order of 0.12 nm. All microstructure measurements were carried out at room temperature. The field-cooled (FC) and the zero-field-cooled (ZFC) magnetization curves were taken with a Quantum Design SQUID magnetometer for the in-plane magnetic field orientation. To avoid the influence of diamagnetic response from LAO, the magnetization curves obtained for the bare substrates were extracted from the raw experimental curves [4].

3. Microstructure of films

Figure 1 shows (a) the high-magnification cross-sectional HREM image and (b) the typical selected-area electron diffraction (SAED) pattern along the [010] zone axes for the BMO film. Because the alternative SAED patterns were not observed, one can conclude that the major phase of the BMO film has the orthorhombic crystal structure with lattice parameters $a \simeq b \simeq 0.56$ nm, $c \simeq 0.7838$ nm and $\alpha = \beta = \gamma \simeq 90°$ which are very close to the published results [20,21]. However, the small regions of long-periodic strip-domain phase, represented by the inset of Fig. 1,*a*, are found as well. In this case the fast Fourier transform (FFT) of HREM image (see Fig. 1,*c*) produces the additional superlattice reflections with a wave vector $q = c^*/3$ (indicated by white arrows), where c^* is the c axis (for cubic symmetry) reciprocal lattice vector. An additional analysis of the HREM images reveals that the strip-domain phase has the orthorhombic crystal symmetry close to the major film's phase.

Figure 2,*a* presents the cross-sectional HREM image for BFMO, including the film/substrate interface. It is seen that

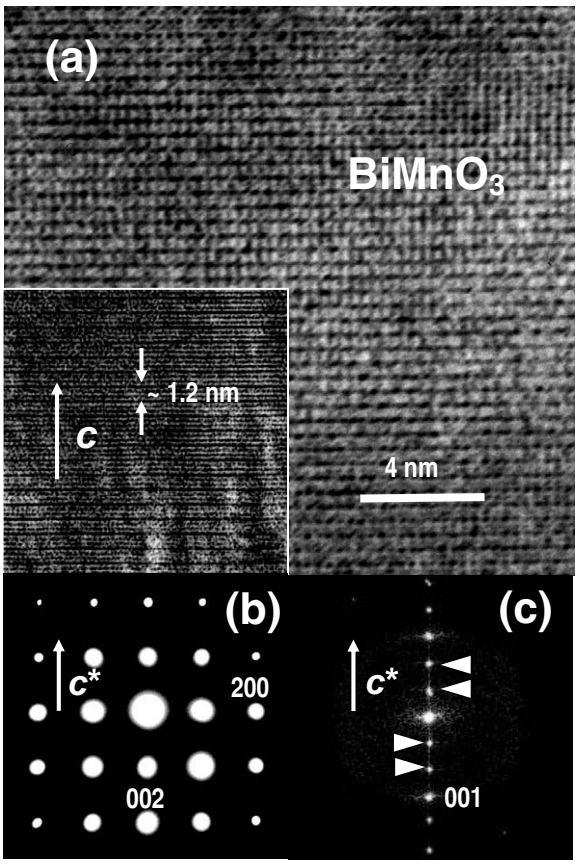

Fig. 1. (*a*) High-magnification cross-sectional HREM image for the BMO film. The inset presents the same image for the strip-domain phase. (*b*) The [010] zone-axis ED pattern for the basic orthorhombic film phase. (*c*) The FFT pattern of HREM image, represented by the inset in *a*. The white arrows show us the period of strip domains. The (001) spot indicates that the strip-domain phase has a crystal lattice of the basic phase.

the film manifests the atomically clean and sharp interface without an amorphous intermediate layer or precipitations. At the same time the statistical SAED analysis reveals three typical ED patterns, which are connected with different orientation of the crystal lattice against to an electron beam direction. Figures 2,*b*, *c* and *d* correspond to SAED patterns along the [100], [001] and [010] zone axes, respectively, for the hexagonal symmetry, represented by Fig. 2,*d*. Therefore, in addition to the predominant *c*-oriented crystal structure the film contains the *a*- and *b*-oriented nanocrystallites. Therefore, according to a microstructure analysis, the prepared BFMO film has the hexagonal crystal structure with lattice parameters $a \simeq b \simeq 0.471$ nm, $c \simeq 0.392$ nm, and the angle between the a and b axes $\gamma \simeq 120°$. Notice that the crystal lattice of this compound is usually indexed as an orthorhombic cell (from x-ray diffraction analysis) [13,15]. Moreover, similar to the BMO film the small-size regions of the strip-domain phase with the 3*c*-periodic spacing, represented by the inset in Fig. 2,*a*, have been observed, as well.

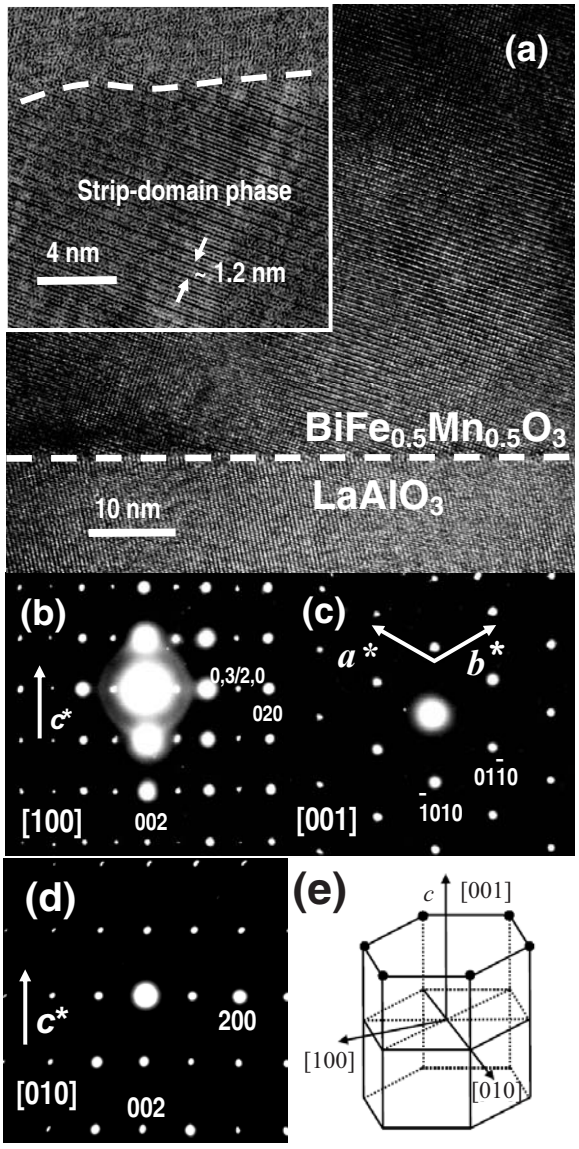

Fig. 2. (*a*) Low-magnification cross-sectional HREM image for the BFMO film. Dashed line indicates the interface between film and substrate. The inset presents the high-magnification HREM image for the strip-domain phase. The dashed line indicates the interphase boundary. (*b*, *c*, and *d*) The selected-area electron diffraction patterns of the BFMO film along the [100], [001] and [010] zone axes, respectively, for the hexagonal symmetry, represented by (*e*).

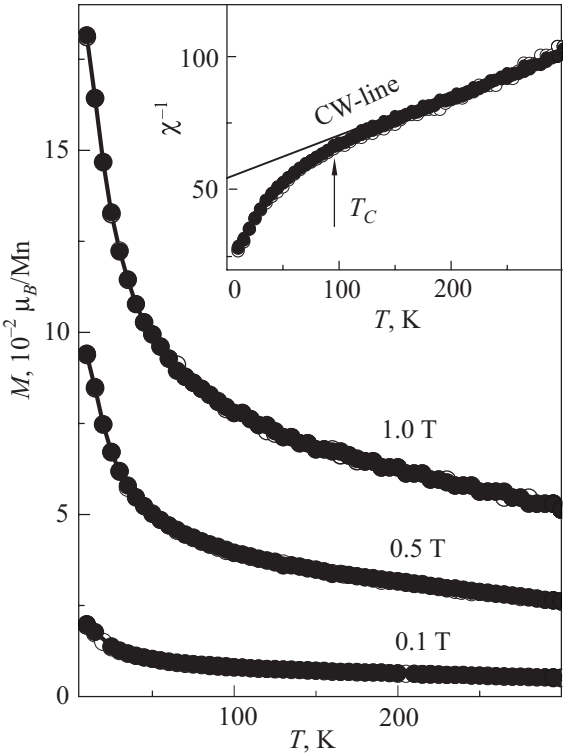

Fig. 3. Temperature dependence of the in-plane FC (solid symbols) and ZFC (open symbols) magnetic moment for the BMO film, measured at different applied magnetic fields. Lines are guides to the eyes. The inset presents the temperature dependence of the inverse dc magnetic susceptibility taken at the same applied fields in ZFC regime. Solid line is the Curie–Weiss linear approximation. The arrow defines an onset of the FM transition.

4. Magnetic properties

Figure 3 shows the in-plane FC and the ZFC temperature dependences of the magnetic moment, $M(T)$, for the BMO film taken at different applied magnetic fields, after an extracting of diamagnetic response from the substrate. Inset displays the temperature dependence of the inverse dc magnetic susceptibility (χ^{-1}) in the dimensionless units taken at the same magnetic fields in ZFC regime. The Curie temperature, $T_C \simeq 105$ K, estimated as a point where the $\chi^{-1}(T)$ curve starts to be deviated from the Curie–Weiss (CW) linear behavior (straight line), is coincident with the published results for bulk [8]. On the other hand, the $M(T)$ behavior at $T \le T_C$ is more typical for the superparamagnetic (SPM) system rather than for a valid ferromagnet, manifesting the smooth exponential increase of the magnetic moment with decreasing temperature. Because $\chi^{-1}(T) \sim (T+\theta)/C_{CW}$ for the PM materials [22], where $C_{CW} = N\mu_{\text{eff}}^2 / 3k_B$ is the CW constant, which is obtained from the experimental curve, θ is the certain characteristic temperature, k_B is the Boltzmann constant, and N is the number of magnetic ions per unit cell, one can estimate the atom's effective magnetic moment in the PM phase, which turn out to be $\mu_{\text{eff}} \simeq 13\ \mu_B$. This value is larger than that is predicted by the CW-theory for a classical PM, $\mu_{\text{eff}}^{\text{theor}} \simeq 4.9\ \mu_B$/Mn, using the expression $\mu_{\text{eff}}^{\text{theor}} = g\sqrt{S(S+1)}$, where $g = 2$ is the Landé factor, and $S = 2$ for Mn^{3+}. A similar PM response with the enhanced magnetic moment has already been observed in the manganites [23] and was attributed to

an existence of the magnetic small-size polarons, which are typical for the diluted magnetic semiconductors.

Figure 4 presents the magnetic hysteresis loops, $M(H)$, for the BMO film at 10 and 300 K after an extracting of diamagnetic response from the substrate. The well-defined linear $M(H)$ dependences testify that the major part of the film stands in the paramagnetic (PM) state at both temperatures with the minor FM contributions (hysteresis terms with a saturation). Insets *a* and *b* display the same dependencies after an extracting of the PM terms more in detail. The hysteresis loops reveal a saturation magnetic moment $M_s \simeq$ 0.0044 and 0.02 μ_B/Mn, a remanent magnetic moment $M_r \simeq$ 0.001 and 0.0016 μ_B/Mn, and a coercive field $H_c \simeq$ 50 and 350 Oe at 300 and 10 K, respectively. It is worth noting that a small FM response is observed at $T >> T_C$, confirming a presence of the small-size FM clusters in the PM matrix.

Figure 5 shows the in-plane FC and the ZFC temperature dependences of the magnetic moment, $M(T)$, for the BFMO film taken at different applied magnetic fields, after an extracting of diamagnetic response from the substrate. The $M(T)$ behavior is very close to that was observed for the BMO film. The linear extrapolation of the $\chi^{-1}(T)$ dependence, represented by inset, reveals that $T_C \simeq$ 150 K, which is coincident with the published results [9,10,16]. The experimental value of $\mu_{\text{eff}} \simeq$ 12 μ_B in the PM phase is also larger of the theoretical one, $\mu_{\text{eff}}^{\text{theor}} \simeq$ 5.9 μ_B/B-site ion. In this case the following expression was used $\mu_{\text{eff}}^{\text{theor}} = g\sqrt{0.5S_1(S_1+1)+0.5S_2(S_2+1)}$, where $S_1 = 2$ and $S_2 = 5/2$ for Mn^{3+} and Fe^{3+} ion, respectively.

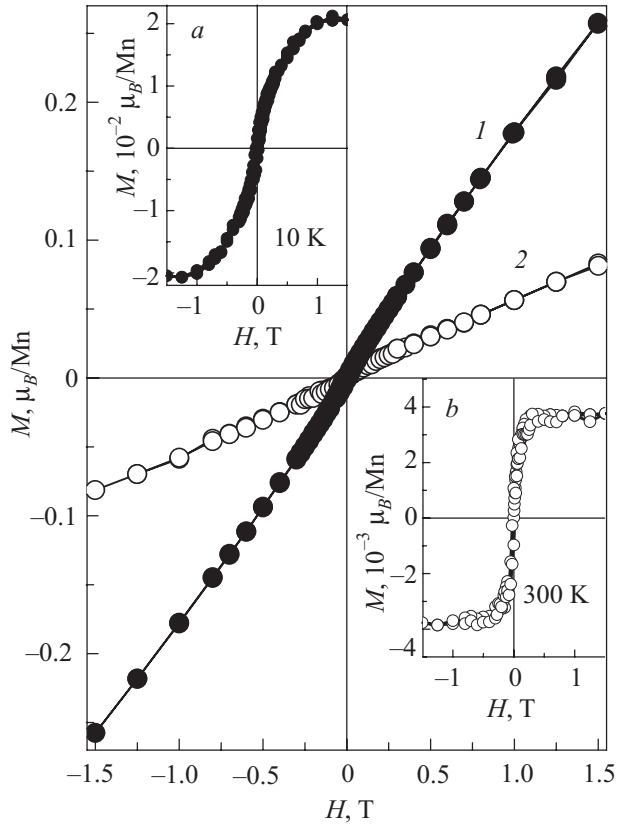

Fig. 4. The in-plane magnetic hysteresis loops for the BMO film taken at T = 10 (*1*) and 300 (*2*) K. Lines are guides to the eyes. The insets *a* and *b* display the same dependencies after an extracting of the PM terms more in detail.

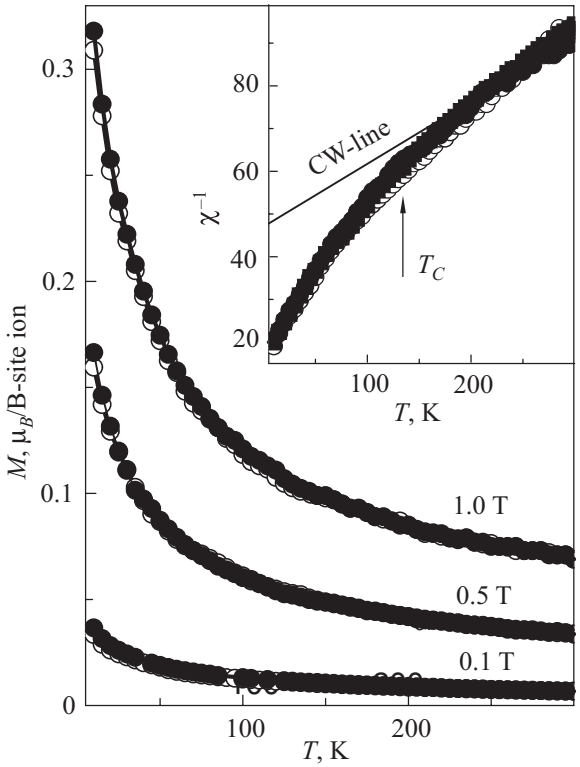

Fig. 5. Temperature dependence of the in-plane FC (solid symbols) and ZFC (open symbols) magnetic moment for the BFMO film, measured at different applied magnetic fields. Lines are guides to the eyes. The inset presents the temperature dependence of the inverse dc magnetic susceptibility taken at the same applied fields in ZFC regime. Solid line is the Curie–Weiss linear approximation. The arrow defines an onset of the FM transition.

Figure 6 presents the magnetic hysteresis loops, $M(H)$, for the BFMO film at 10 and 300 K after an extracting of diamagnetic response from the substrate. Once again, similar to BMO, the $M(H)$ behavior is typical for the multiphase magnetic system which contains the PM (linear term) and the FM (hysteresis term with a saturation) contributions. Insets *a* and *b* display the same dependencies after an extracting of the PM linear terms more in detail. The hysteresis loops rerveal a saturation magnetic moment $M_s \simeq 0.01$ and $0.06\mu_B$/B-site ion, a remanent magnetic moment $M_r \simeq$ 0.002 and $0.0075\mu_B$/B-site ion, and a coercive field $H_c \simeq$ 150 and 400 Oe at 300 and 10 K, respectively. A small FM response is observed at a room temperature ($T >> T_C$), as well, verifying the exis-

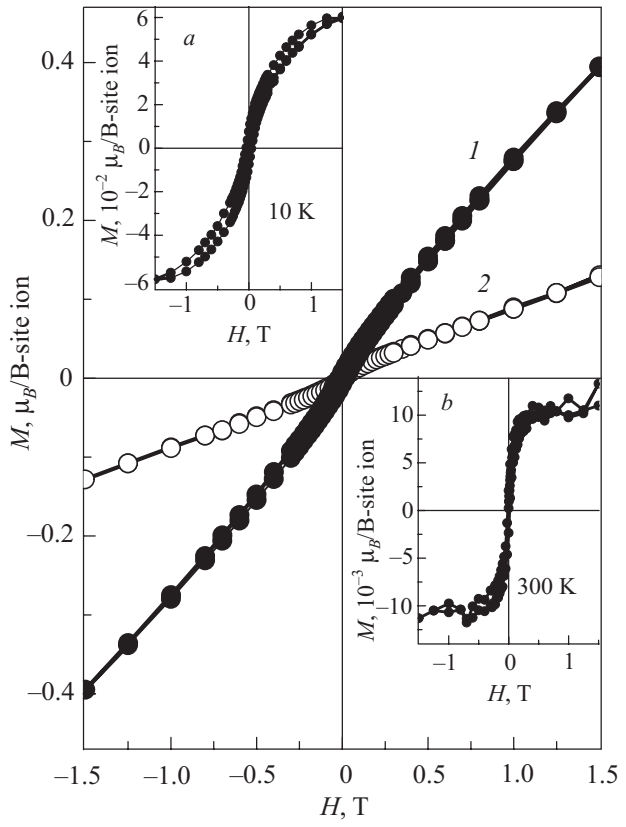

Fig. 6. The in-plane magnetic hysteresis loops for the BFMO films taken at T = 10 (*1*) and 300 (*2*) K. Lines are guides to the eyes. The insets *a* and *b* display the same dependencies after an extracting of the PM terms more in detail.

tence of the FM clusters with the enhanced magnetic moment in the PM matrix.

5. Discussion

The experimental data reveal that the orthorhombic BMO and hexagonal BFMO films remain in the PM phase throughout the whole investigated temperature interval. At the same time, an appearance of the small FM response with the nontypical for FMs $M(T)$ behavior deserves further discussion. The PM background of the films is confirmed by the lack of the ZFC/FC $M(T)$ splitting at low temperature (see Figs. 3 and 5), but should be observed in the AFM matrix with the FM entities through the exchange-bias interaction.

In spite of that the FM transition starts at 105 and 150 K in the BMO and BFMO films, respectively, the complete long-range FM order does not observe up to lowest temperature. Moreover, the hysteresis loops with a saturation magnetic moment are observed at $T >> T_C$ (insets *b* in Figs. 4 and 6). Such kind of a magnetic behavior is typical for the percolation system and should be considered in the context of a Griffiths-like model which predicts an appearance of the FM clusters in the temperature range $T_C(p_c) \le T \le T_G$, where $T_C(p_c)$ is the actual Curie temperature, provided by a percolation threshold, and T_G is the highest achievable critical temperature [24]. In this case we deal with the first-order magnetic transition in which disorder has driven $T_C(p_c)$ to 0 K and the inverse susceptibility could be described by the power law: $\chi^{-1} \sim [T/T_C(p_c) - 1]^{1-y}$, where $y \le 1$ [25,26]. The logarithmic plots, presented by the insets in Fig. 7, are a fit of the data to this power law with the result that $y = 0.66$ and 0.45, and $T_C(p_c) = 3$ and 1 K, for the BMO and BFMO films, respectively. The obtained results well agree with the theoretical predictions and confirm the percolation origin of the FM transition in the investigated films. The Griffiths phase can be treated formally as an assembly of the magnetic polaron clusters in diluted magnetic semiconductors [27], with the following temperature dependence of the magnetic moment: $M(T,H) = M(0,H)\exp(-k_BT/\mu_{\text{eff}}H)$, where $M(0,H)$ is the magnetic moment at T = 0 K and μ_{eff} is the effective magnetic moment of magnetic polaron cluster. Therefore, the total value of the magnetic susceptibility for the BMO and BFMO films can be expressed by $\chi(T,H) = \chi_0^G \exp(-k_BT/\mu_{\text{eff}}H) + C_{CW}/(T+\theta)$, where χ_0^G is the susceptibility of the Griffiths phase at T = 0 K. The first term belongs to the FM clusters (Griffiths phase) while the second one corresponds to the major PM part of the sample. Figure 7 present the ZFC $\chi(T)$ dependences for BMO and BFMO taken at different applied magnetic field: H = 0.1 (solid circle), 0.5 (open circle) and 1.0 T (solid square). The solid lines are theoretical curves constructed with the fitting parameters of $\chi_0^G = 0.028$ and 0.03 in the dimensionless units, and $\mu_{\text{eff}} = 350$ and 450 μ_B for BMO and BFMO, respectively. The PM term was obtained from the linear extrapolation of the $\chi^{-1}(T)$ experimental curves, represented by the insets in Figs. 3 and 5. It is seen that the theoretical curves excellently agree with the experimental ones. Because the theoretical average magnetic moment of 4.9 and 5.4 μ_B/B-site ion for BMO and BFMO, respectively, the estimated average diameter of a magnetic polaron cluster in the Griffiths phase turns out to be $D \simeq$ 2 nm.

In spite of that measured films have the different crystal lattice — the orthorhombic and hexagonal ones — the same microstructure peculiarity is observed in the both cases. There is a strip-domain phase with the periodic spacing of about 3*c*. We argue that this low-dimensional layered structure is a genuine origin of the weak ferromagnetism in the BMO and BFMO films through the formation of the Griffiths-phase state. It should be noted that a similar phenomenon has already been observed in the hole-doped manganite films where an appearance of the long-periodic strip-domain structure is attributed to a specific ordering between the rare-earth and doped ions [28,29]. However, in our case the strip-domain phase rather governed by the cooperative Jahn–Teller effect since Mn^{3+} and Fe^{3+} belong to so-called Jahn–Teller-kind ions and have a tendency to the charge and orbital ordering [30].

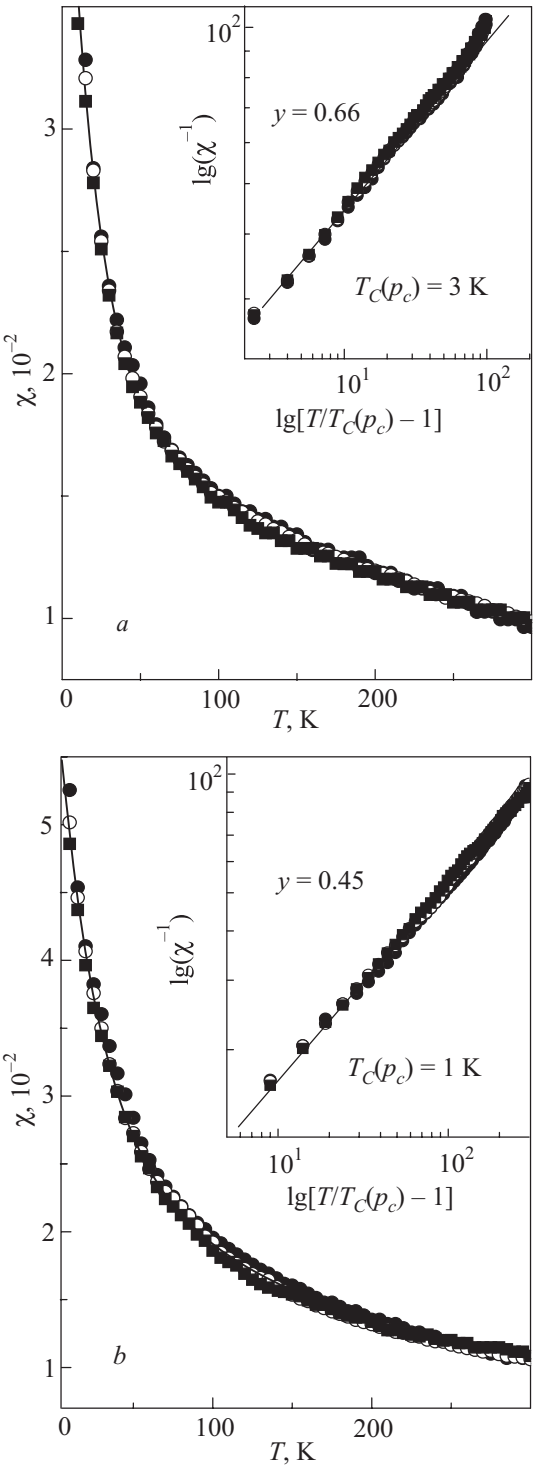

Fig. 7. Temperature dependence of the in-plane ZFC magnetic susceptibility for the BMO (*a*) and BFMO (*b*) films, measured at different applied magnetic fields. The solid line is the theoretical curve obtained within the framework of the Griffiths-phase model. The inset presents the logarithmic plot of the inverse susceptibility versus normalized temperature. The solid straight line is a fit of the experimental data to a percolation power law, discussed in the text.

Conclusions

In summary, the $BiMnO_3$ and $BiFe_{0.5}Mn_{0.5}O_3$ films have been prepared by the rf magnetron sputtering on $LaAlO_3$ (001) single-crystalline substrate. The selected-area electron diffraction analysis allows us to identify the crystal structure of the $BiMnO_3$ film as an orthorhombic one while the $BiFe_{0.5}Mn_{0.5}O_3$ film has a hexagonal lattice symmetry. The high-resolution electron-microscopy study reveals the presence of strip-domain phase with a periodic spacing of about 3*c* in both films. The magnetic measurements show that in addition to the basic paramagnetic phase, the films manifest the Griffiths phase behavior in a wide temperature range. Therefore, the weak ferromagnetism observed in the $BiMnO_3$ and $BiFe_{0.5}Mn_{0.5}O_3$ films is provided by an appearance of the strip-domain layered phase rather than intrinsic physical origin.

Acknowledgments

This work was supported by the NRF/MEST through the Quantum Photonic Science Research Center, Korea. V. Svetchnikov is grateful to the financial support of the Netherlands Institute for Metal Research.

1. X. Qi, J. Dho, R. Tomov, M.G. Blamire, and J.L. MacManus-Driscoll, *Appl. Phys. Lett.* **86**, 062903 (2005).
2. W. Eerenstein, F.D. Morrison, J. Dho, M.G. Blamire, J.F. Scott, and N.D. Mathur, *Science* **307**, 1203a (2005).
3. N.A. Spaldin and M. Fiebig, *Science* **309**, 391 (2005).
4. V.G. Prokhorov, G.G. Kaminsky, J.M. Kim, T.W. Eom, J.S. Park, Y.P. Lee, V.L. Svetchnikov, G.G. Levtchenko, Yu.M. Nikolaenko, and V.A. Khokhlov, *Fiz. Nizk. Temp.* **37**, 161 (2011) [*Low Temp. Phys.* **37**, 129 (2011)].
5. C. Ederer and N. Spaldin, *Phys. Rev.* **B71**, 069401 (2005).
6. I. Dzyaloshinskii, *J. Phys. Chem. Solids* **4**, 241 (1958).
7. T. Moria, *Phys. Rev.* **120**, 91 (1960).
8. F. Sugawara, S. Iida, Y. Syono, and S. Akimoto, *J. Phys. Soc. Jpn.* **20**, 1529 (1965).
9. A.F. Moreira dos Santos, S. Parashar, A.R. Raju, Y.S. Zhao, A.K. Cheetham, and C.N.R. Rao, *Solid State Commun.* **122**, 49 (2002).
10. A.F. Moreira dos Santos, A.K. Cheetham, W. Tian, X. Pan, Y. Jia, N.J. Murphy, J. Lettieri, and D. Schlom, *Appl. Phys. Lett.* **84**, 91 (2004).
11. Z.H. Chi, H. Yang, S.M. Feng, F.Y. Li, R.C. Yu, and C.Q. Jin, *J. Magn. Magn. Mater.* **310**, 358 (2007).
12. T. Shishidou, N. Mikamo,Y. Uratani, F. Ishii, and T. Oguchi, *J. Phys.*: *Condens. Matter* **16**, S5677 (2004).
13. M. Azuma, H. Kanda, A.A. Belik, Y. Shimakawa, and M. Takano, *J. Magn. Magn. Mater.* **310**, 1177 (2007).
14. L. Bi, A.R. Taussing, H.S. Kim, L. Wang, G.F. Dionne, D. Bono, K. Persson, G. Ceder, and C.A. Ross, *Phys. Rev.* **B78**, 104106 (2008).

15. P. Mandal, A. Sundaresan, C.N.R. Rao, A. Iyo, P.M. Shirage, Y. Tanaka, Ch. Simon, V. Pralong, O.I. Lebedev, V. Caignaert, and B. Raveau, *Phys. Rev*. **B82**, 100416 R (2010).
16. Y. Du, Z.X. Cheng, S.X. Dou, X.L. Wang, H.Y. Zhao, and H. Kimura, *Appl. Phys. Lett*. **97**, 122502 (2010).
17. E.M. Choi, S. Patnaik, S.-L. Sahonta, H. Wang, Z. Bi, J. Xiong, M.G. Bamire, Q.X. Jia, and J.L. MacManus-Driscoll, *Appl. Phys. Lett*. **98**, 012509 (2011).
18. J. Miao, X. Zhang, Q. Zhan, Y. Jiang, and K.-H. Chew, *Appl. Phys. Lett*. **99**, 062905 (2011).
19. V.N. Varyukhin, Yu.V. Medvedev, Yu.M. Nikolaenko, A.B. Mukhin, B.V. Belyaev, V.A. Gritskikh, I.V. Zhikharev, S.V. Kara-Murza, N.V. Korchikova, and A.A. Tikhii, *Technical Phys. Lett.* **35**, 937 (2009).
20. H. Yang, Z.H. Chi, J.L. Jiang, W.J. Feng, Z.E. Cao, T. Xian, C.Q. Jin, and R.C. Yu, *J. of Alloys and Compounds* **461**, 15 (2008).
21. A.A. Belik, K. Kodama, N. Igawa, S. Shamoto, K. Kosuda, and E. Takayama-Muramachi, *J. Am. Chem. Soc*. **132**, 8137 (2010).
22. B.D. Cullity, *Introduction to Magnetic Materials*, Addison-Wesley, New York (1972).
23. J.A. Souza, J.J. Neumeier, and Y.K. Yu, *Phys. Rev*. **B78**, 014436 (2008).
24. R.B. Griffiths, *Phys. Rev. Lett*. **23**, 17 (1969).
25. A.J. Bray, *Phys. Rev. Lett*. **59**, 586 (1987).
26. A.H. Castro Neto, G. Castilla, and B.A. Jones, *Phys. Rev. Lett*. **81**, 3531 (1998).
27. V.M. Galitski, A. Kaminski, and S.D. Sarma, *Phys. Rev. Lett*. **92**, 177203 (2004).
28. Y.H. Hyun, J.S. Park, T.W. Eom, G.H. Kim, Y.S. Lee, Y.P. Lee, V.G. Prokhorov, and V.L. Svetchnikov, *Appl. Phys. Lett*. **93**, 042515 (2008).
29. T.W. Eom, Y.H. Hyun, J.S. Park, Y.P. Lee, V.G. Prokhorov, V.S. Flis, and V.L. Svetchnikov, *Appl. Phys. Lett*. **94**, 152502 (2009).
30. M.J. Calderón, A.J. Millis, and K.H. Ahn, *Phys. Rev*. **B68**, 100401(R) (2003).